Ter-diurnal Atmospheric Tide on Mars

Joonas Leino[1], Ari-Matti Harri[1], Robert John Wilson[2], Don Banfield[3], Mark Lemmon[4], Mark Paton[1], Jose-Antonio Rodriguez-Manfredi[5], Hannu Savijärvi[1,6]

[1]Finnish Meteorological Institute, Helsinki, Finland
[2]NASA Ames Research Center, Moffett Field CA, USA
[3]Cornell University, Cornell Center for Astrophysics and Planetary Science, Ithaca, NY, USA
[4]Space Science Institute, Boulder, CO, USA
[5]Centro de Astrobiologia (INTA-CSIC), Madrid, Spain
[6]Institute for Atmospheric and Earth System Research, Helsinki, Finland

Key Points:

- We analyze ter-diurnal atmospheric tide from MSL, InSight, VL1, and VL2 observations and compare them with GCM predictions
- GCM underestimates observed values and it predicts a clear wavenumber 6 amplitude pattern in longitude during northern hemisphere summer
- This study suggests ter-diurnal component's sensitivity to water ice clouds and a resonantly-enhanced Kelvin wave near NH summer solstice

Corresponding author: Joonas Leino, joonas.leino@fmi.fi

Abstract

Cyclic absorption of solar radiation generates oscillations in atmospheric fields. These oscillations are called atmospheric or thermal tides, which are furthermore modified by topography and surface properties. This leads to a complex mix of sun-synchronous and non sun-synchronous tides that propagate around the planet eastward and westward. This study focuses on analyzing the ter-diurnal component (period of 8 hr) from surface pressure observations by Mars Science Laboratory (MSL), InSight, Viking Lander (VL) 1, and VL2. General Circulation Model (GCM) results are used to provide a global context for interpreting the observed ter-diurnal tide properties. MSL and InSight have a clear and similar seasonal cycle, with local amplitude peaks at around solar longitude (Ls) 60°, Ls 130° and Ls 320°. The amplitude peak at Ls 320° is related to the annual dust storm, while the dust storm around Ls 230° is not detected by either platforms. During the global dust storms, MSL, VL1, and VL2 detect their highest amplitudes. GCM predicts the weakest amplitudes at the equinoxes, while the strongest ones are predicted in summertime for both hemispheres. GCM amplitudes are typically lower than observed, but match better during the aphelion season. During this time, model results suggest that the two most prominent modes are the sun-synchronous ter-diurnal tide (TW3) and an eastward propagating resonantly-enhanced Kelvin wave (TE3). Simulations with and without the effect of radiative heating by water ice clouds indicate the clouds may play a significant role in forcing the ter-diurnal tide during northern hemisphere summer season.

Plain Language Summary

Atmospheric pressure is crucial meteorological parameter, since many weather phenomena on Mars, such as the condensation and sublimation of the seasonal polar caps, global scale atmospheric tides, and local turbulent flows are associated with changes in surface pressure. On a diurnal time scale, atmospheric tides dominate surface daily pressure variations in Martian tropics. They are generated by the diurnal solar radiation and additionally modified by topography, surface properties, and atmospheric dust content. Here we use pressure observations from Mars Science Laboratory, InSight, Viking lander 1, and 2 to determine Martian atmospheric tide that has a period of 8 hr, known as ter-diurnal tide. Furthermore, model simulations are used to compare the results. The results show that Mars Science Laboratory and InSight have a similar seasonal cycles for the amplitude and phase of the ter-diurnal tide. In addition, both of them react similarly to atmospheric dust content. Viking landers and Mars Science Laboratory observe their highest amplitudes during the global dust storms. We find that modeling amplitudes are the strongest during summertime for both hemispheres and typically lower than those observed throughout the year. Moreover, ter-diurnal tide may be significantly affected by water ice clouds.

1 Introduction

Atmospheric tides or thermal tides are global oscillations in atmospheric fields, e.g. pressure, temperature, and wind fields. They are generated by the cyclic absorption of solar radiation which leads to oscillations that are integer fractions of a solar day. The first four components are diurnal (period of 24 hour), semi-diurnal (period of 12 hour), ter-diurnal (period of 8 hour) and quad-diurnal (period of 6 hour) harmonics. Direct solar radiation leads to a westward propagating migrating tides and the interaction with the topography, surface properties (e.g. thermal inertia and albedo), and atmospheric absorbers (mainly dust on Mars) can generate either eastward or westward propagating non-migrating tides. On Mars, these tides are a big part of the atmospheric circulation (e.g. Zurek, 1976; Hamilton, 1982; Wilson & Hamilton, 1996; Banfield et al., 2000) but on Earth, they are only relevant in the upper atmosphere (e.g. Hagan & Roble, 2001).

Diurnal and semi-diurnal tides in the Martian atmosphere are quite deeply studied (e.g. Zurek, 1976; Leovy & Zurek, 1979; Hamilton, 1982; Wilson & Hamilton, 1996; Guzewich et al., 2016) but the ter-diurnal tide has received much less attention due to its weaker nature. The same applies for the Earth due to very small amplitudes, but some studies of the ter-diurnal atmospheric tide exists. Most of these studies on Earth focus on upper atmospheric wind and temperature measurements (e.g. Smith, 2000; Moudden & Forbes, 2013), however, Ray et al. (2023) studied these tides extracted from the European Centre for Medium-Range Weather Forecasts ERA5 reanalysis atmospheric surface pressure data.

A major aspect of the study is to obtain some global insight into the Martian atmospheric ter-diurnal oscillations seen at a very small collection of lander sites (e.g. Leovy, 1981; Guzewich et al., 2016; Viúdez-Moreiras et al., 2020). In this investigation, we study the ter-diurnal tide and its behavior during the year and with different atmospheric dust contents. We use Mars Science Laboratory (MSL), InSight, Viking Lander 1 (VL1), and VL2 surface pressure observations to calculate ter-diurnal amplitudes and phases. Moreover, we utilize Mars Climate Database (MCD) General Circulation Model (GCM) global surface pressure fields in the interpretation of the results and global properties of the ter-diurnal tide on Mars.

The structure of this work is as follows. In Section 2 we describe possible generation mechanisms of the ter-diurnal tide. In addition, we shortly describe the used data and methods to investigate the ter-diurnal component. In Section 3 we show the observed ter-diurnal tides for each station. Section 4 includes a comparison of the MCD GCM and observed tides as well as analyze of different modes. Finally, we summarize and discuss the results in Section 5.

2 Ter-diurnal Tide and Data

2.1 Ter-diurnal Tide

The terrestrial ter-diurnal surface pressure tide is dominated by the migrating component (TW3) and is primarily forced by absorption of solar radiation by ozone and water vapor (Siebert, 1961; Groves & Wilson, 1982). Ter-diurnal forcing is fundamentally meridionally antisymmetric, in contrast to the diurnal tide and all the even harmonics (semi-diurnal, quad-diurnal, etc). Thus the TW3 would be expected to be strongest in the solstice seasons, with a minimum in the equinoctial seasons. The dominant antisymmetric mode of the ter-diurnal response peaks at roughly 30 degrees latitude. The latitude asymmetry is mirrored in the semiannual variation in the phase at midlatitudes.

Recently, Ray et al. (2023) provided ter-diurnal amplitudes on Earth from the European Centre for Medium-Range Weather Forecasts ERA5 reanalysis data. Their results suggest that the highest amplitudes are expected in wintertime for both hemispheres. In addition, they found amplitudes almost disappearing during both equinoxes and peaking in midlatitudes during solstices.

On Mars, direct solar forcing and nonlinear interactions between diurnal (zonal wavenumber 1) and semi-diurnal (zonal wavenumber 2) tides can be the most dominant forcing mechanisms of the migrating ter-diurnal tide (e.g. Viúdez-Moreiras et al., 2020). Migrating diurnal zonal wavenumber 1 and semi-diurnal zonal wavenumber 2 tides are typically the most dominant components on Mars (e.g. Wilson & Hamilton, 1996; Guzewich et al., 2016). Therefore, nonlinear interaction between these tides can have a very large effect on the amplitude of the near-surface ter-diurnal tide.

In the Martian atmosphere, non-migrating tides play also a huge role. They can propagate eastward or westward and are not sun-synchronous. They are forced by the interaction of the radiation with zonal inhomogeneities in topography, surface proper-

ties, and atmospheric absorber concentration (e.g. Wilson & Hamilton, 1996). For example, the interaction of the diurnal westward-migrating solar radiation with the zonal wavenumber 2 topography generates diurnal westward propagating wavenumber 3 (DW3) and diurnal eastward propagating wavenumber 1 (DE1) tides (e.g. Forbes et al., 2002). For the semi-diurnal forcing, zonal wavenumber 4 topography generates westward propagating wavenumber 6 (SW6) and eastward propagating wavenumber 2 (SE2) components. Respectively, ter-diurnal radiational forcing interacting with wavenumber 6 topography would produce westward propagating wavenumber 9 (TW9) and eastward propagating wavenumber 3 (TE3) components. All these possible interactions described above can be verified with basic trigonometric identities (e.g. Forbes et al., 2002; Read & Lewis, 2004).

2.2 Observations and Methods

The Viking mission was the first successful mission on the surface of Mars (Chamberlain et al., 1976; Hess et al., 1977). It included two landers, Viking Lander 1 and 2 (VL1 and VL2) that landed on Mars in Martian year (MY) 12. The locations were Chryse Planitia (22.48°N, 310.03°E) and Utopia Planitia (47.97°N, 134.26°E) for the VL1 and VL2, respectively. They measured pressure, temperature, wind speed, and wind direction. It should be noted that the VL record is complicated by the significant quantization of the observations and the presence of significant gaps in the coverage (e.g. J. E. Tillman et al., 1993). The lack of precision compromises extracting low amplitude tide harmonics in the aphelion season. However, we suppose that the tide is relatively well-behaved, but its hard to cleanly extract this signal from the available data.

The Mars Science Laboratory (MSL) Curiosity rover landed on Mars in MY 31. At the time of writing, it has operated near the equator within the Gale Crater (4.6°S, 137.4°E) for almost six full Martian years. Air pressure (Harri et al., 2014) is measured by the Rover Environment Monitoring Station (REMS) instrument (Gómez-Elvira et al., 2012) which also includes humidity, ground and air temperature, wind velocity, and ultraviolet sensors. The pressure is measured typically in 5-minute blocks every hour but also in extended, one-to-three-hour blocks.

The InSight lander landed relative close to MSL on Elysium Planitia (4.5°N, 135.6°E) in MY 34. It measured air pressure constantly with very high frequency (Spiga et al., 2018) for over one MY and reached the end of its mission at the early MY 36. These constant measurements are extremely useful for observing weather phenomena on different time scales, such as short duration pressure drops (Spiga et al., 2021), global atmospheric tides (Viúdez-Moreiras et al., 2020; Leino et al., 2023), as well as seasonal and diurnal pressure cycles (Viúdez-Moreiras et al., 2020; Leino et al., 2023).

Here we investigate the ter-diurnal harmonic component using a Fast Fourier Transform (FFT). The approach is similar as in Leino et al. (2023). For each weather station, the input data was binned into one hour intervals based on local true solar time (LTST) and we used a window of three sols to get at least one observation for each hour. The binned value was averaged in case of multiple observations per hour. Amplitudes and phases were then calculated for the middle sol of the three-sol window. This procedure assumes that the three consecutive sols are similar enough for calculating the harmonic component with a period of 8 hours. The analysis was performed for each station by sliding the three-sol window over all the pressure data that was available for each platform.

For the MCD GCM surface pressure data, we used a similar approach except that one-sol window was used for each location. Global coverage allows us to also decompose the pressure field into westward and eastward propagating components (Section 4). That was done by taking a 2D FFT (in time and longitudes) for the diurnal pressure fields.

2.3 Mars Climate Database

The Mars Climate Database (MCD) is a database of meteorological fields from Laboratoire de Météorologie Dynamique (LMD) General Circulation Model (GCM) simulations of the Martian atmosphere (Forget et al., 1999; Millour et al., 2017). The MCD includes dust scenarios from MY 24 to MY 35, which are produced from the dust observations made by Thermal Emission Spectrometer (TES, aboard Mars Global Surveyor), the Thermal Emission Imaging System (THEMIS, aboard Mars Odyssey), and the Mars Climate Sounder (MCS, aboard Mars Reconnaissance Orbiter) (Montabone et al., 2015, 2020). The resolution of the LMD GCM is 5.625° in longitude and 3.75° in latitude, but MCD includes a "high-resolution mode" to compute surface pressure as accurately as possible. The "high-resolution mode" combines the LMD GCM surface pressures with the high resolution (32 pixels per degree) MOLA topography and the smoothed InSight pressure records. In this study, we use MY 35 dust scenario and the "high-resolution mode" to extract the MCD surface pressures. These global GCM fields allow for mapping of the evolving tide harmonic results and, further, decomposing these into constituent eastward and westward propagating components. Moreover, we use special GCM simulations with and without the effect of radiative heating by water ice clouds provided by the LMD team.

3 Observed Surface Pressure Ter-diurnal Tides

Ter-diurnal amplitudes and phases for the MSL, InSight, VL1, and VL2 as a function of the season (Ls) are shown in Figures 1 and 2, respectively. MSL shows quite clear seasonal cycle with amplitudes reaching first maximum around Ls 60° (∼3 Pa). After a small drop a second maximum is observed at around Ls 130° (∼3 Pa). After the second peak, MSL observes very sharp drop with a minimum amplitudes near Ls 160° (∼0.5 Pa). Thereafter amplitudes start to rise slowly until about Ls 300° where typically the highest amplitudes are around 4 Pa. After that, a high peak (∼5 Pa) is observed each year at around Ls 315°–325°. Amplitudes decrease the rest of the year and reach very low values (typically less than 0.5 Pa) around Ls 15°–30°. MY 34 has one unique feature, the global dust storm. During that time, MSL observed ter-diurnal amplitudes higher than 11 Pa.

InSight shows very similar yearly pattern as the MSL but it also shows a slightly more pronounced peak in amplitude (∼3.5 Pa) at Ls 40°. During MY 34, the peak in amplitude at about Ls 320° is however smaller at InSight (∼5 Pa) compared to MSL (∼8 Pa) location. During MY 35, the same annual spike is also smaller at the InSight location. These clear yearly amplitude patterns shown by the MSL and InSight are quite different compared to diurnal and semi-diurnal components which are very sensitive to local/regional and global atmospheric dust loading (Chapman & Lindzen, 1970; Wilson & Hamilton, 1996; Guzewich et al., 2016; Zurita-Zurita et al., 2022; Wilson & Kahre, 2022; Leino et al., 2023). Moreover, the seasonality of the ter-diurnal tide is quite different for that of the other higher harmonic even tides: migrating quad- and hexa-diurnal tides, which tend to maximize in the equinoctial season. In addition, the dust forcing of these even modes is clearly indicated in Figure 1 in Wilson et al. (2017).

The VL1 tide response shows a high degree of repeatability from year to year during the Ls 0°–135° season, consistent with the high regularity seen at the MSL and InSight. This early year pattern includes two clear peaks at around Ls 45°–60° and Ls 125°, with amplitudes greater than 3.5 Pa. Both landers, VL1 and VL2, observe very high amplitudes during the MY 12 global planet-encircling 1977b dust storm around Ls 275°–300°. VL1 observed amplitudes greater than 8 Pa while VL2 observed amplitudes grater than 12 Pa during the storm. Interestingly, ter-diurnal component does not show indication of the 1977a dust storm, while semi-diurnal amplitude shows a strong response during that time (Leovy, 1981; Wilson & Hamilton, 1996). In addition to this, VL1 observed amplitudes of about 8 Pa during the MY 15 dust storm at around Ls 210°–220°.

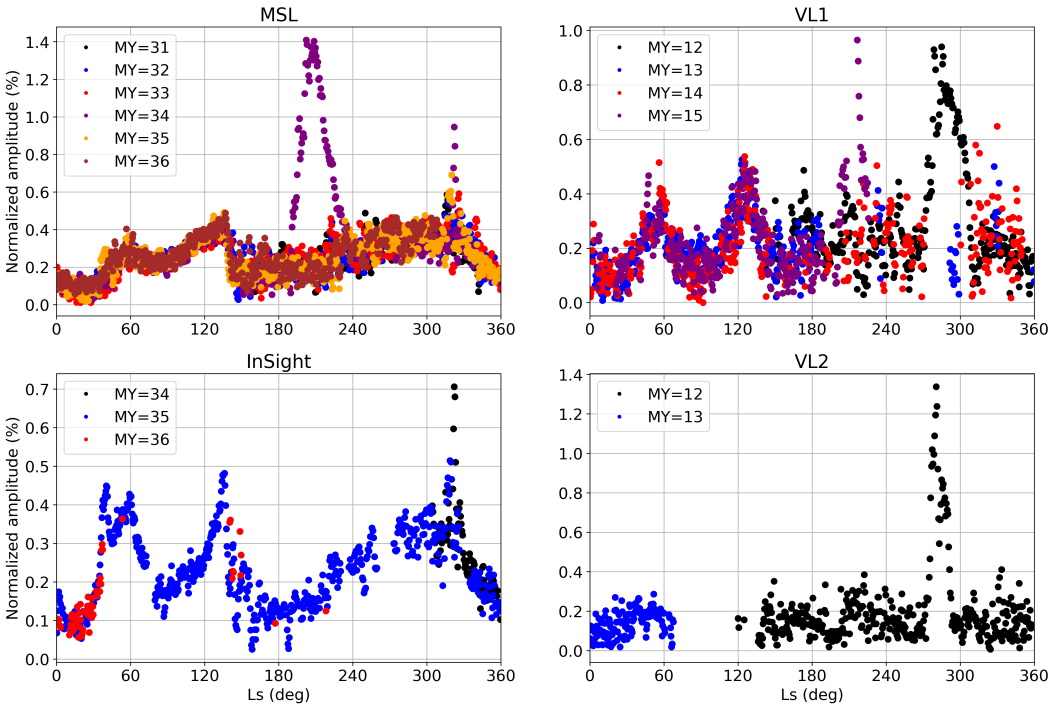

Figure 1. Ter-diurnal amplitudes (normalized by the diurnal mean pressure, %) from the MSL (upper left), InSight (bottom left), VL1 (upper right) and VL2 (bottom right) observations as a function of the season (Ls).

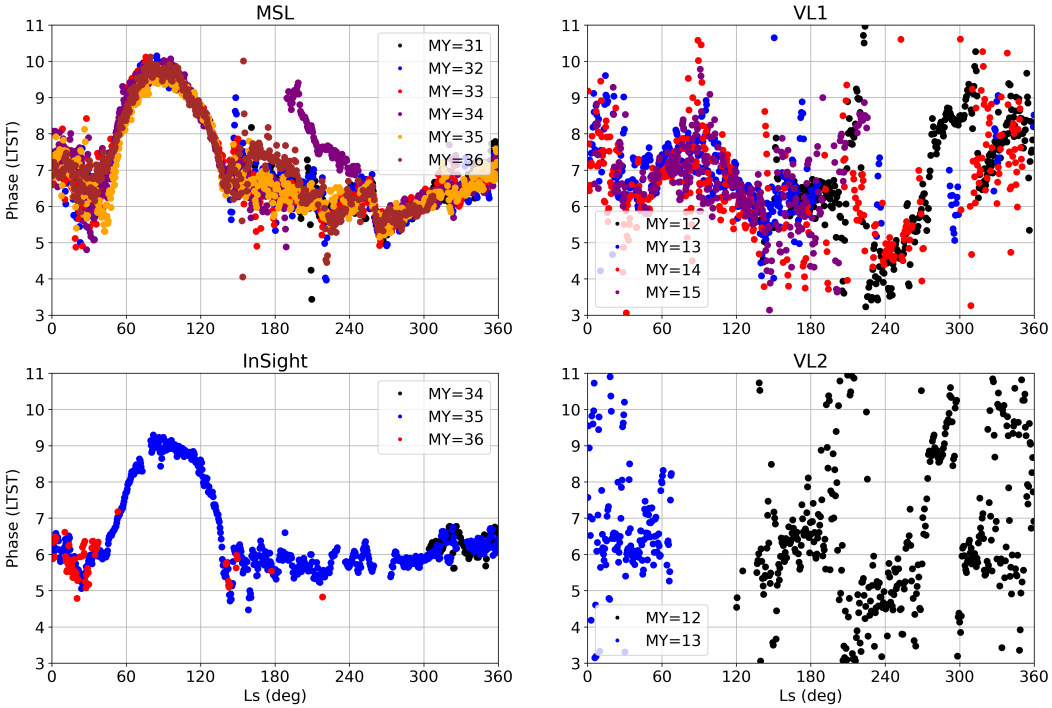

Figure 2. The same as Figure 1 but for the ter-diurnal phases (LTST).

VL2 amplitudes are very chaotic and they do not show any clear patterns, except during the dust storm.

MSL and InSight also show a clear seasonal patter in ter-diurnal phases (Figure 2). The phase for the MSL varies more but the pattern is quite similar. Both stations observe phases of around 08–10 LTST from Ls 60° to Ls 120° and around 05–07 LTST for the rest of the year. This delay and advance suggests the increasing presence of the resonantly-enhanced ter-diurnal Kelvin wave as will be discussed later. Some seasonal behavior in the VL1 phases can also be seen but with much more variability compared to the seasonal cycles of the MSL and InSight. In addition, the pattern is different than that for the MSL and InSight. However, VL1 also shows signs of phase delay and advance during Ls 60°–120°. On the other hand, VL2 does not show any clear patterns.

Figure 3 shows the MSL Mastcam dust optical depths during the MSL mission, except the MY 34 due to the global dust storm. A first clear increase in dust optical depths is shown about Ls 135°–150°, but ter-diurnal amplitudes are decreasing during that time (Figure 1). Second increase in atmospheric dust content is captured from about Ls 180° to about Ls 240°. During that time ter-diurnal amplitudes also increase quite fast. Nonetheless, as the atmospheric dust content decreases thereafter, ter-diurnal amplitude continues to increase until about Ls 300°, when dust content reaches its local minimum.

For each year, highest optical depths are measured at about Ls 230° and another peak at about Ls 320°. These dust storms are categorized as "A" and "C" storms, respectively (Kass et al., 2016). They are regular planet encircling or regional-scale southern hemisphere dust storms, but annual variation is higher for "C" storms. Interestingly, MSL and InSight (Figure 1) show a clear amplitude peak only during the "C" dust storm, but no distinct spike is observed during the "A" storm, although diurnal and semi-diurnal

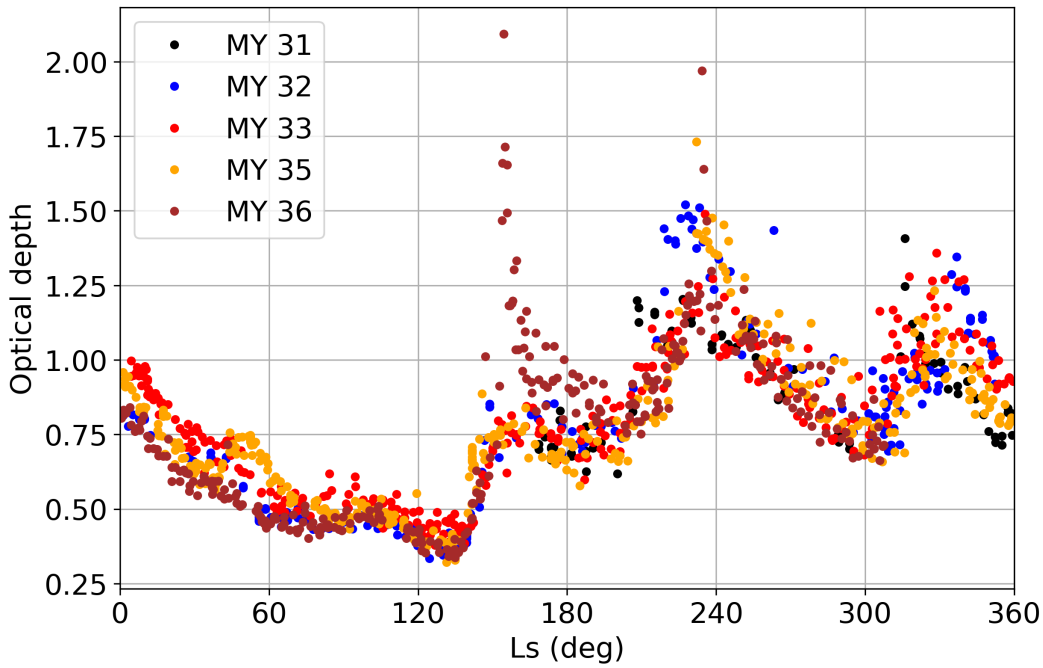

Figure 3. Mastcam optical depths as observed by Mars Science Laboratory (MSL) as a function of season (Ls) during the mission. MY 34 is not shown due to the global dust storm.

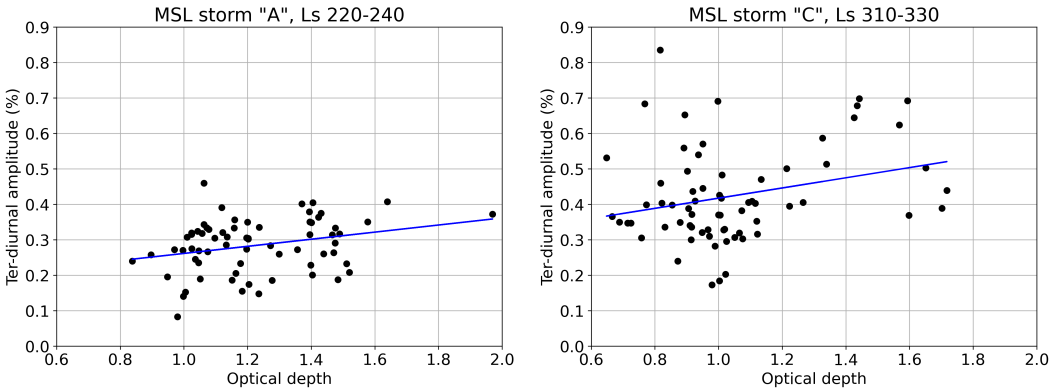

Figure 4. Ter-diurnal amplitudes (%) from the Mars Science Laboratory (MSL) observations as a function of daily average MSL Mastcam optical depths during annual dust storm "A" (Ls 220°–240°, left) and "C" (Ls 310°–330°, right). A linear fit to the data is also shown for each season separately (blue lines).

components showed a clear amplitude peak during the "A" dust storm as well (Leino et al., 2023).

Comparison between MSL observed ter-diurnal amplitudes and Mastcam daily averaged optical depths during these two annual dust storms is shown in Figure 4. Much higher amplitudes as well as more variation is visible during the "C" dust storm. It should be noted that the highest ter-diurnal amplitudes do not necessarily correspond to exactly the same sols as the highest dust optical depths. As an example, during the MY 35 "C" dust storm, the highest optical depth was measured at about Ls 328° (MSL sol 2965) while the highest ter-diurnal amplitude was detected already at about Ls 320° (MSL sol 2951). Similar behavior of the diurnal tide amplitude was found in (Leino et al., 2023). Initially-localized dust event will excite a range of non-migrating tide components, which can contribute to constructive or destructive interference at a given longitude. This is particularly prominent with the short-lived excitation of a diurnal Kelvin wave during regional dust storms (Wilson & Kahre, 2022).

4 Comparing Observed Ter-diurnal Tides with Model Data

Contoured maps of ter-diurnal tide amplitudes at each point from the MCD throughout MY 35 in steps of Ls 30° is presented in Figures 5 and 6. Amplitudes are the weakest at the equinoxes (Ls 0° and Ls 180°) and the strongest from northern hemisphere summer solstice (Ls 90°) until Ls 120°, rather similarly as on the Earth (Ray et al., 2023). During the northern hemisphere summer season, the highest amplitudes are predicted in the latitude range of about 15°S–45°N. During the southern hemisphere summer season, the highest amplitudes are predicted in the latitude range of about 60°S–0°S, but some high amplitude areas are also visible at latitudes of about 15°N–45°N. By contrast, recent study by Ray et al. (2023) showed the highest amplitudes in wintertime for both hemispheres.

An obvious wavenumber 6 pattern is visible at the northern hemisphere from Ls 60° to Ls 150°. During Ls 240°–300°, the wavenumber pattern at the southern hemisphere is not so clear, however. A wavenumber 5 pattern is probably the most apparent during that time period. Such behavior is somewhat different than for the diurnal and semi-diurnal components. They appear to exhibit similar patterns throughout the

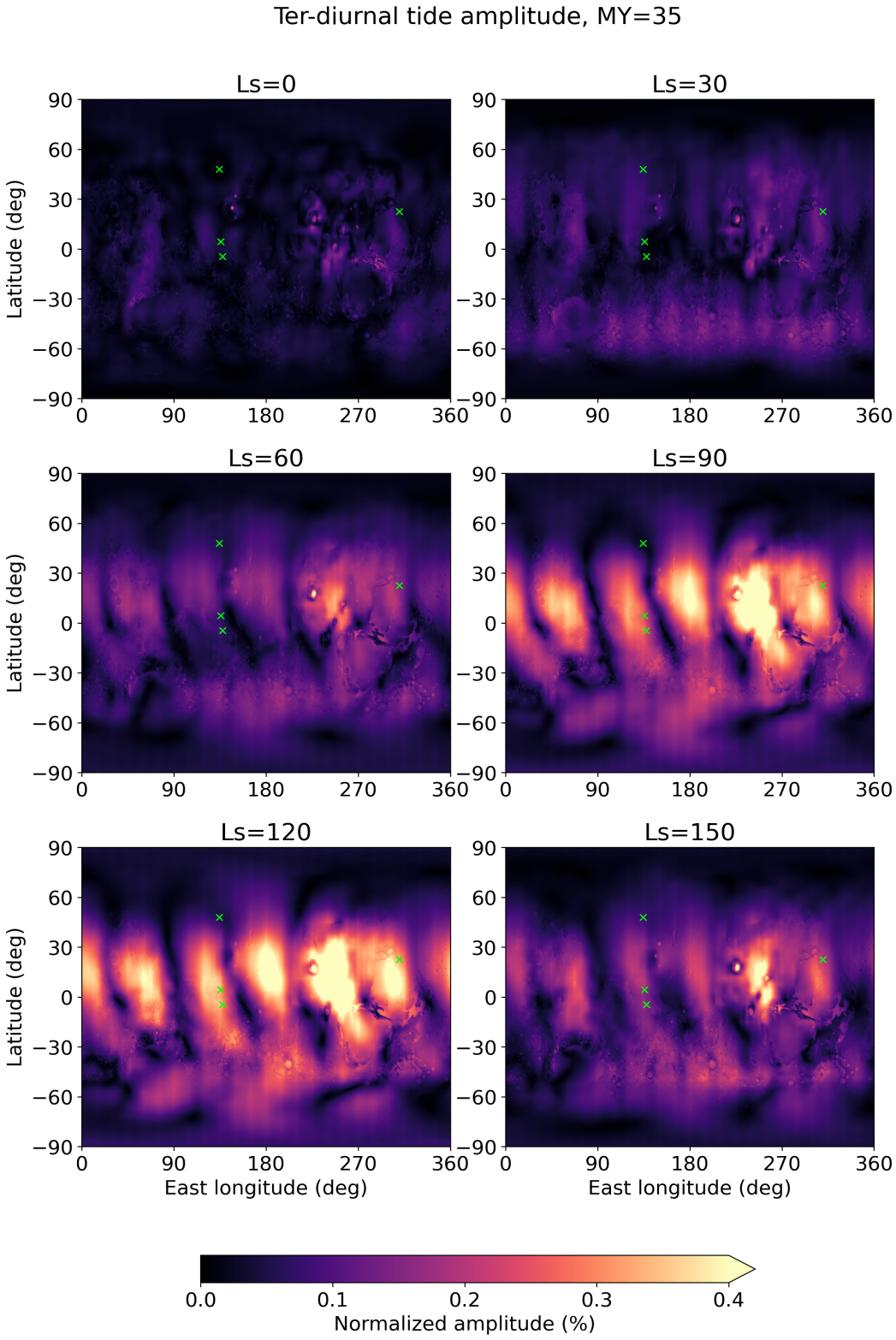

Figure 5. Global ter-diurnal tide normalized amplitudes from the Mars Climate Database for Ls 0°–150°. The location of each platform is marked with a green cross.

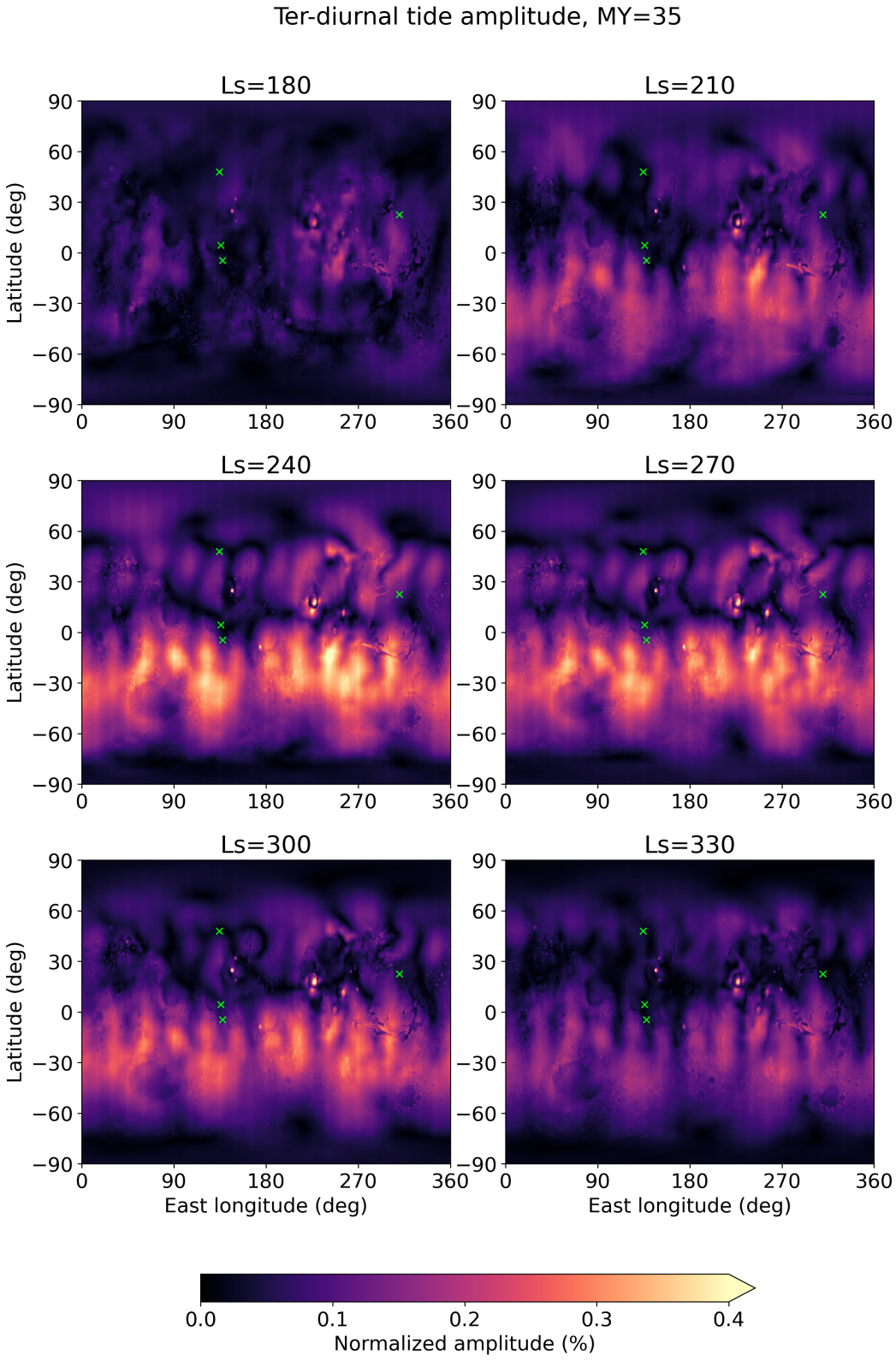

Figure 6. The same as Figure 5 but for Ls 180°–330°.

year, zonal wavenumber 2 and 4 pattern for the diurnal and semi-diurnal components, respectively (Wilson & Hamilton, 1996; Guzewich et al., 2016).

MSL (4.6°S, 137.4°E) and InSight (4.5°N, 135.6°E) are located slightly south from the maximum of the wavenumber 6 pattern at Ls 60° and Ls 150°, but at Ls 90° and Ls 120°, they are located just on the maximum amplitude. During the southern hemisphere summer, they are located somewhat north from the maximum amplitude of the wavenumber 5 pattern.

VL1 (22.48°N, 310.03°E) is located at the edge of the northern hemisphere wavenumber 6 pattern maximum from Ls 60° to Ls 150°. During other time periods, it is located in the area of low amplitudes. VL2 (47.97°N, 134.26°E) is, nonetheless, located in the area of low amplitudes throughout the year.

Ter-diurnal amplitudes and phases from the observations and MCD at each locations are shown in Figures 7 and 8, respectively. Leino et al. (2023) showed close matches between the diurnal and semi-diurnal amplitudes from the MCD and measured by the MSL and InSight. By contrast, MCD ter-diurnal amplitudes for each location here are typically lower than observed ones, especially at the end of the year. On the other hand, MCD phases provide quite close matches for the observations, expect for the MSL.

The MCD simulation produces only one strong amplitude peak for the MSL, InSight, and VL1 locations. The peak reaches its maximum amplitude at Ls 110°, slightly earlier than the second observed peak at about Ls 125°–130°. After the peak, MCD amplitudes start to decrease similarly to the observed ones until about Ls 160°. After that, MCD continues to produce relative good matches with MSL observations until about Ls 220°. However, the rest of the year, simulated amplitudes are much lower than the ob-

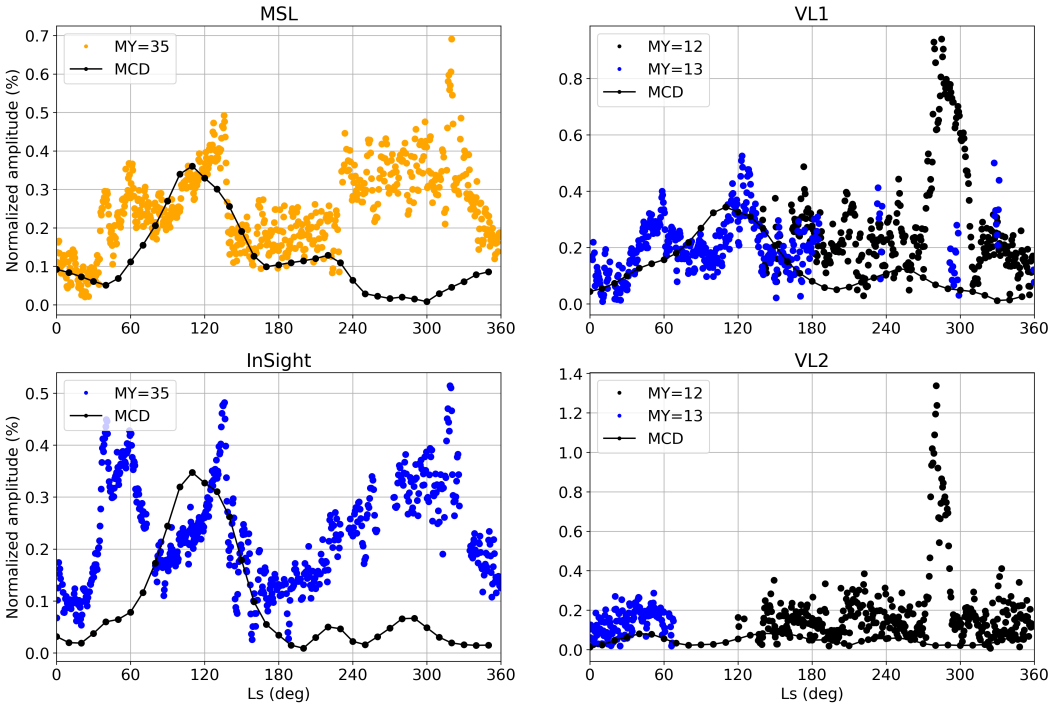

Figure 7. Ter-diurnal amplitudes (%) from MSL (upper left), InSight (bottom left), VL1 (upper right) and VL2 (bottom right) observations as well as from MCD as a function of the season (Ls).

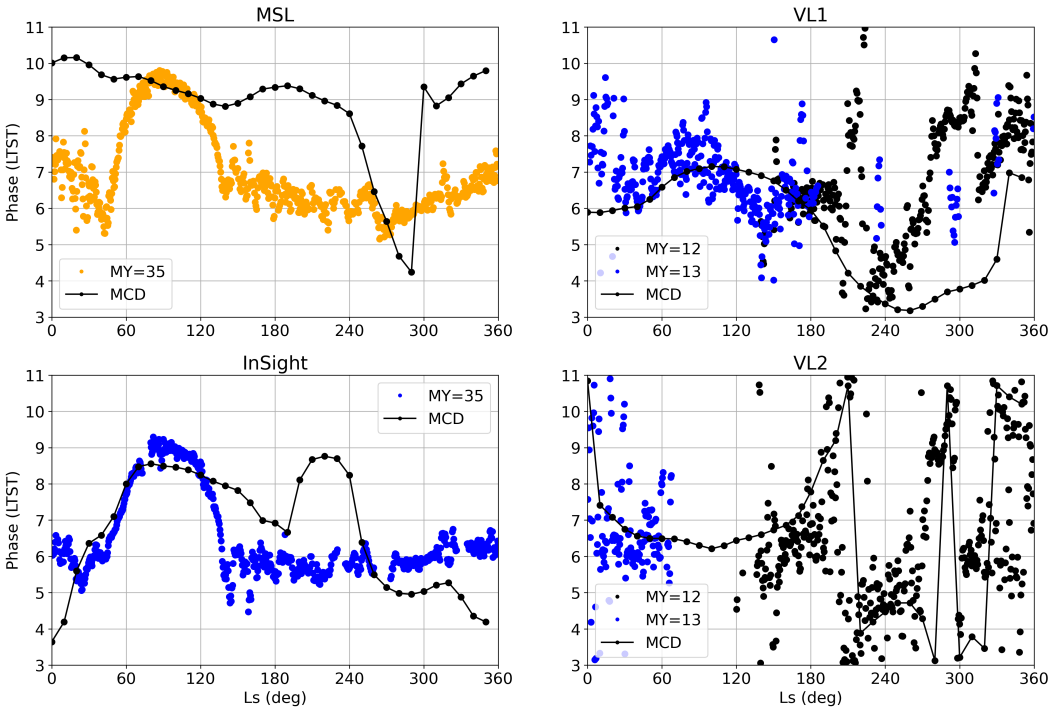

Figure 8. The same as Figure 7 but for the ter-diurnal phases (LTST).

served ones. For the InSight, MCD amplitudes start to deviate from the observations from about Ls 200° onwards. For the VL2, MCD produces much lower amplitudes than observed ones throughout the year.

Globally, MCD suggests the lowest amplitudes near the equinoxes (Figures 5 and 6), which is in relatively good agreement with observations. Slightly shifted simulated amplitude patterns in longitude or extended in latitude during the first half of the year could yield better matches in the individual locations. The rest of the year, global amplitude maps from the MCD are lacking a clear structure and each of these weather stations are located in the areas of low amplitude. The areas nearby the MSL and InSight have slightly higher amplitudes but still much smaller than observed. Therefore, MCD seems to produce relatively reliable ter-diurnal amplitudes during the first half of the year but the rest of the year is unclear due to small amount of measurement stations on the surface.

MCD ter-diurnal amplitudes for zonal wavenumbers 1–4 for westward (TW, left panel) and eastward (TE, right panel) propagating tides for Ls 0°, Ls 90°, Ls 180° and Ls 270° are shown in Figure 9. Two particularly prominent tide modes are present: westward propagating migrating zonal wavenumber 3 (TW3) and eastward propagating non-migrating zonal wavenumber 3 (TE3). TW3 has maxima about 10–30 degrees off of the equator in the solstice seasons. By contrast, the TE3 tide is most prominent during the northern hemisphere summer solstice season.

In the Ls 90° season, the TW3 and TE3 modes have comparable amplitude between 20°S–0°S, which leads to maximal constructive/destructive interference in this latitude range. This accounts for the zonal wave 6 modulation in ter-diurnal amplitude seen in the spatial maps at Ls 60°–150° (Figure 5). The meridional structure of TE3 is characteristic of a Kelvin wave, with a uniform latitude structure. This structure may be a

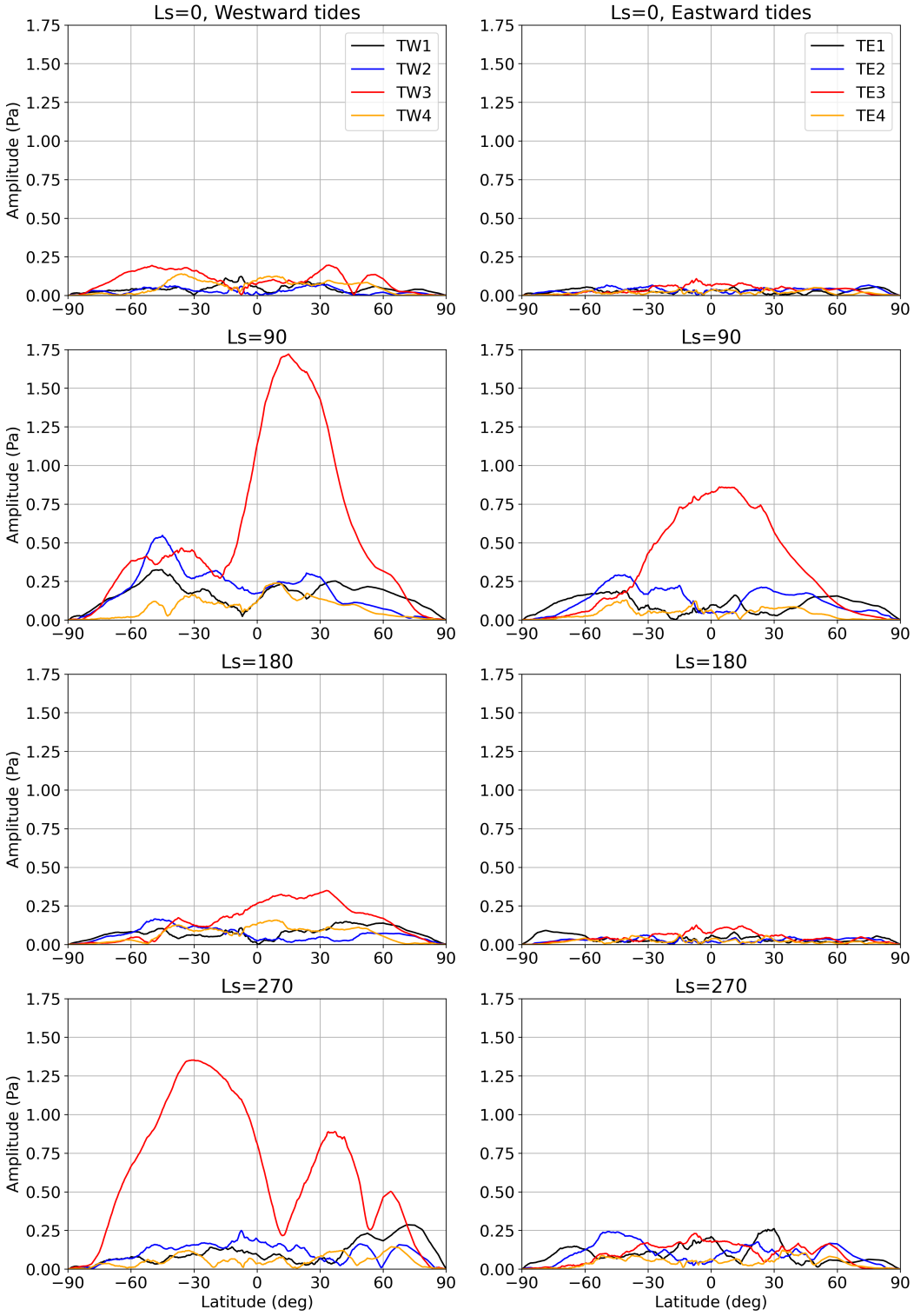

Figure 9. Ter-diurnal amplitudes (Pa) for the westward (TW, left panel) and eastward (TE, right panel) propagating zonal wavenumber 1–4 components as a function of latitude from the MCD for Ls 0° (first row), Ls 90° (second row), Ls 180° (third row) and Ls 270° (fourth row).

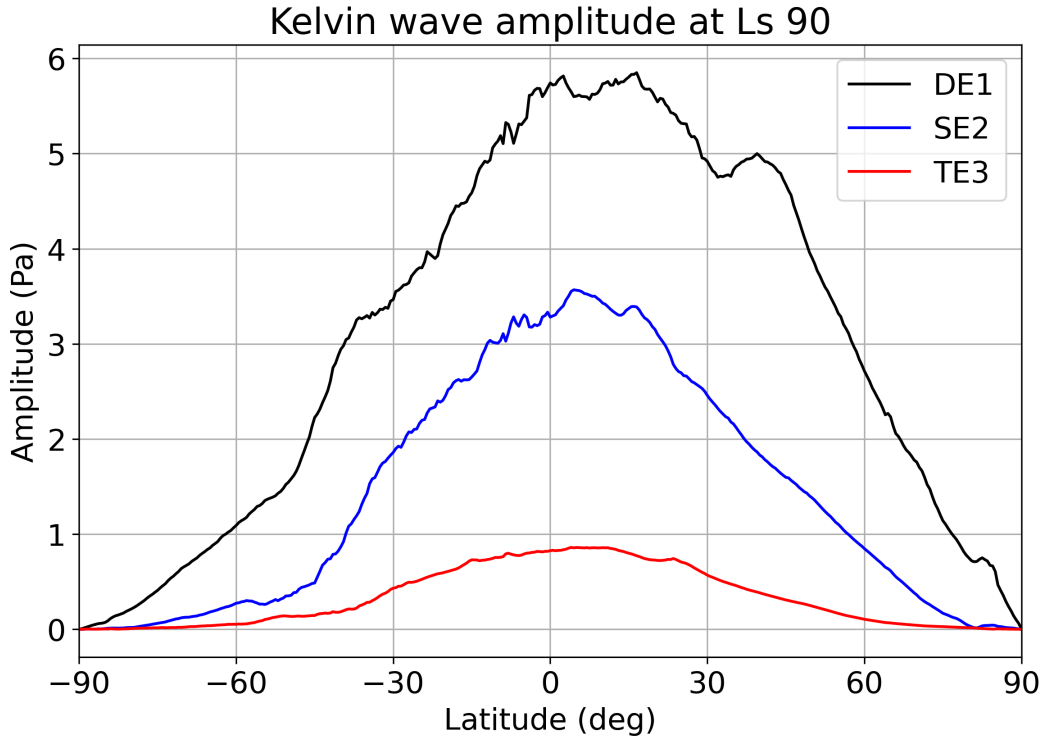

Figure 10. Mars Climate Database diurnal (DE1, black), semi-diurnal (SE2, blue), and ter-diurnal (TE3, red) Kelvin wave amplitudes at Ls 90°.

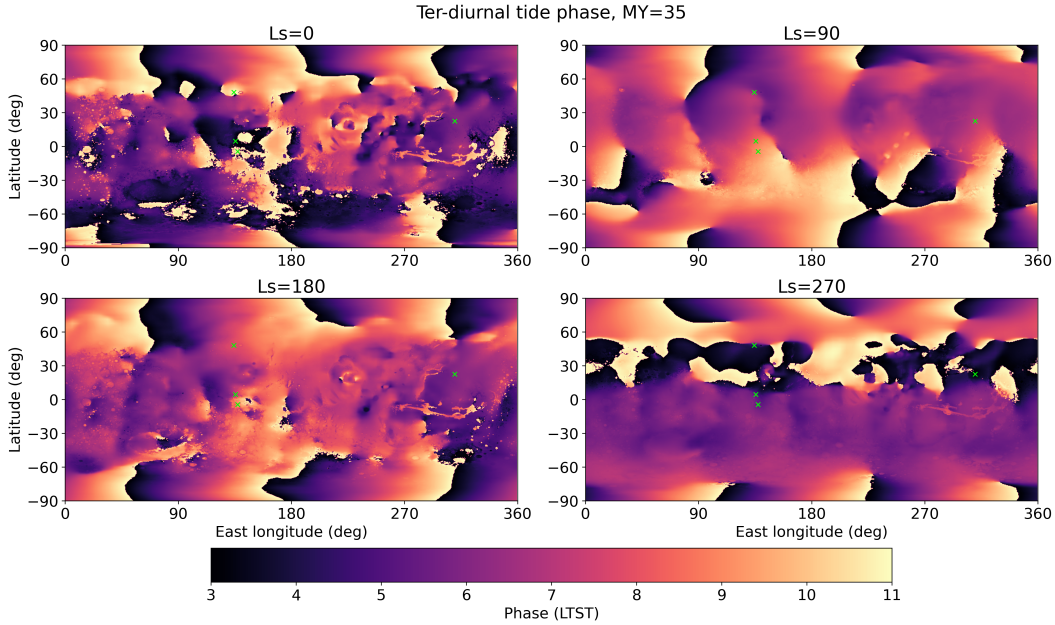

Figure 11. Global ter-diurnal tide phases from the Mars Climate Database for Ls 0°, Ls 90°, Ls 180°, and Ls 270°. The location of each platform is marked with a green cross.

result of zonal wavenumber 6 inhomogenities in the topography, and is very similar to that of DE1 and SE2 which are also prominent in the MCD simulation (Figure 10).

Ter-diurnal global phases obtained from the MCD are shown in Figure 11. As expected from the amplitude pattern (Figure 5), the phase pattern has a similar zonal wave 6 modulation at Ls 90°. This suggests that phases at the locations of MSL, InSight, VL1, and Perseverance (Fig. 7, Harri et al., 2024) would vary in sync over the annual cycle if the TW3/TE3 tide component were dominant. As suggested by Figures 5 and 9, this takes place during northern hemisphere summer season, which is also supported by observations (Figures 1 and 2).

Moreover, Figure 11 shows some asymmetry between north and south and between summer and winter. Ray et al. (2023) found that on Earth ter-diurnal tide is peaking at the solstice seasons near 02 LTST in winter and 06 LTST in summer seasons, and the wave disappears during each equinox. These properties are similar as here, since Figures 5 and 6 showed the disappearance of the ter-diurnal tide during each equinox and Figure 11 indicates phase asymmetry. The TW3 mode is particularly dominant during the southern hemisphere summer solstice season, which dominates the amplitude and phase structure, so that they are more zonally uniform (strongest at about 30°S, Figure 11) than other seasons.

Figure 12 shows the relationship between ter-diurnal amplitude, dust column visible optical depth, and water ice column from the MCD at the locations of MSL (upper left), InSight (lower left), VL1 (upper right), and VL2 (lower right) during MY 35. It clearly shows the sensitivity of the predicted ter-diurnal amplitude in column water ice during the first half of the year, when local airborne dust conditions are relatively low and constant. Ter-diurnal amplitudes follow more airborne dust conditions during the second half of the year. However, ter-diurnal amplitude peak at the locations of MSL

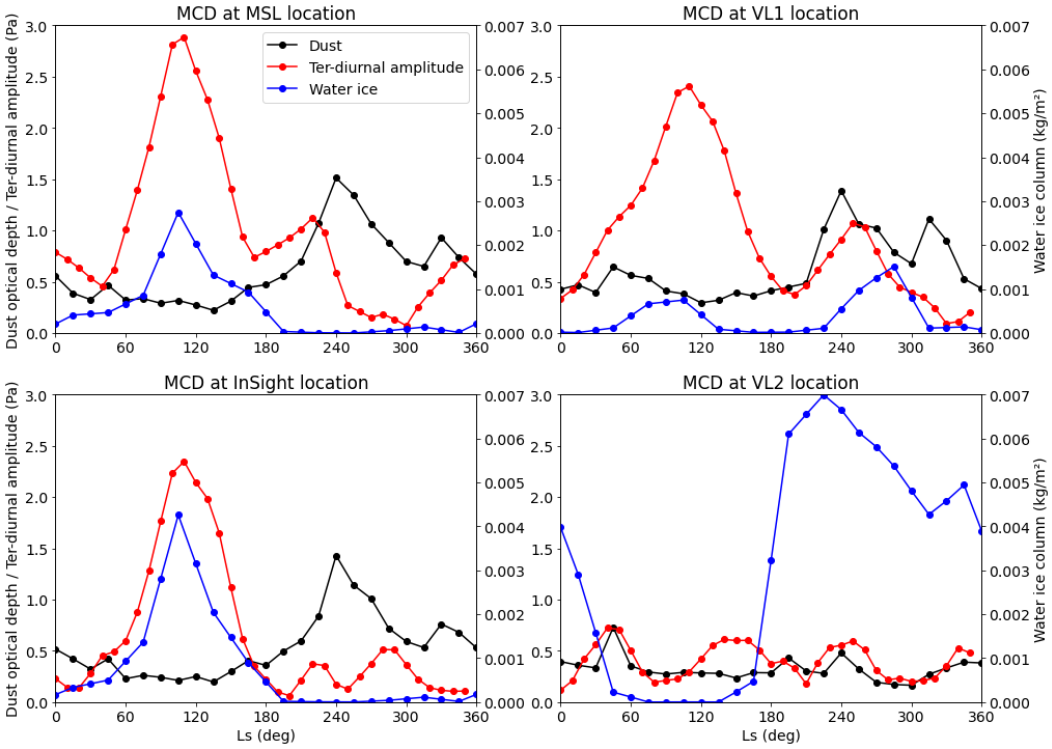

Figure 12. Ter-diurnal amplitude (Pa, red), daily mean dust column visible optical depth above surface (black), and water ice column (kg/m^2, blue) from MCD at the MSL (upper left), InSight (lower left), VL1 (upper right), and VL2 (lower right) locations during MY 35.

and InSight is reached somewhat earlier (at about Ls 220°) than the first local dust peak (Ls 240°). On the other hand, the second ter-diurnal amplitude peak at the MSL location is reached after the local dust peak.

The seasonal evolution of the TW3 (upper, a) and TE3 (lower, c) amplitudes are shown in Figure 13, which also shows the dust column opacity contours (upper, a) and water ice cloud contours (lower, c) with contour intervals of 0.25 and 0.5 pr-μm, respectively. TE3 tide amplitude peaks at the equator near Ls 90° with low amplitudes for the rest of the year. Therefore, TE3 has the amplitude characteristic of the resonantly-enhanced ter-diurnal Kelvin wave, essentially analogous to the DE1 and SE2 that are also present in the simulations (Wilson et al., 2017). The delay and advance of the observed (MSL, InSight, and VL1) ter-diurnal phases from Ls 60° to Ls 120° in Figure 2 is consistent with the increasing presence of the ter-diurnal Kelvin wave. TW3 response is, on the other hand, stronger away from the equator, and this mode is present for a much longer fraction of the year. The influence of dust forcing on TW3 is much more evident in the dusty season. In particular, Figure 13a shows two regional dust storms in MY 35 corresponding to "A" and "C" flushing-storm events.

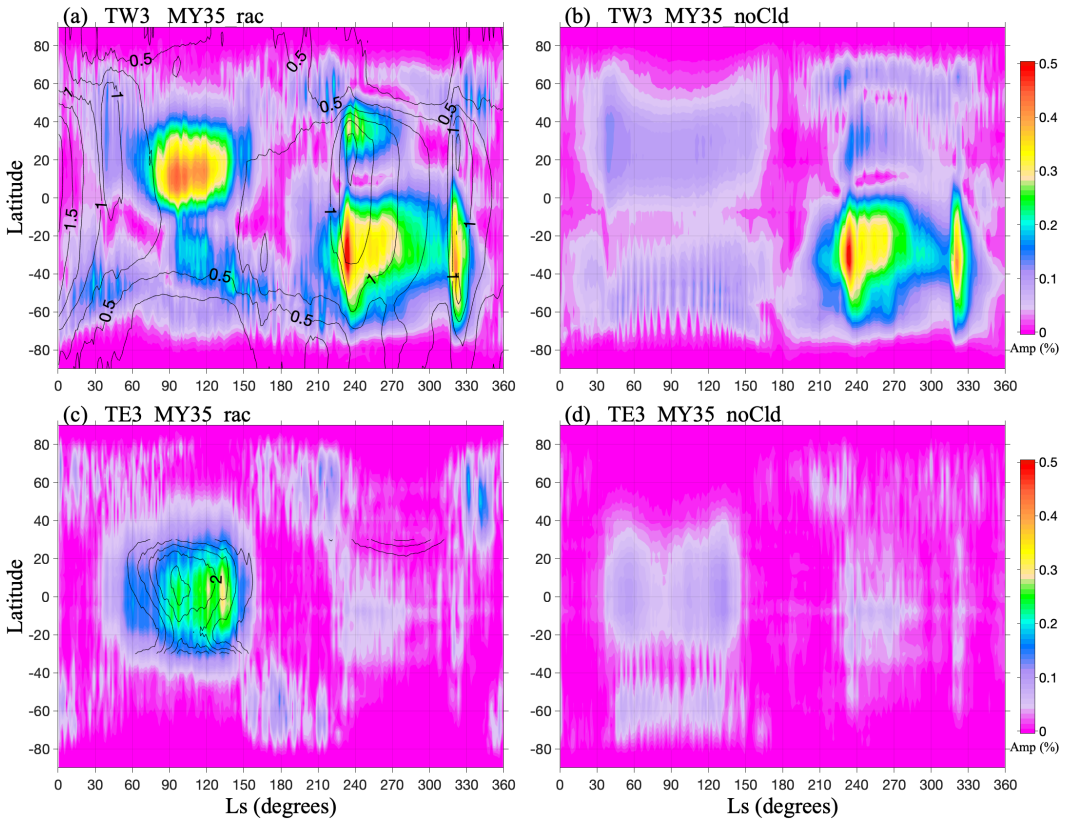

Figure 13. Seasonal normalized amplitude evolution of TW3 (upper) and TE3 (lower) modes with (left panel) and without (right panel) the effect of radiative heating by water ice clouds from the LMD GCM simulation. Dust column opacity contours are shown on the TW3 field (a) and water ice cloud contours are shown on the TE3 field (c). The contour intervals are 0.25 for the dust opacity and 0.5 pr-μm for the water ice column. Cloud column contours are limited to the tropics to avoid the very thick polar hood clouds.

To study the effect of water ice clouds more deeply, LMD team provided us a GCM simulation with the radiative effect of clouds turned off (Figure 13 b and d). Clearly the clouds are having an influence. TE3 is much less prominent in a simulation without radiatively active water ice clouds. In addition, TW3 amplitude is weaker during the aphelion season, especially at the northern hemisphere. Thus, water ice clouds play a prominent role in forcing the TW3 tide response in the first half of the Mars year. Their heating projects onto a mix of symmetric and antisymmetric modes, with the maximum response present north of the equator. The modulation of the directly-forced TW3 tide with wavenumber 6 forcing (due to topography and a wave 6 component of the cloud field) leads to the excitation of the near-resonant Kelvin wave component of TE3, which is a symmetric mode. Therefore, these simulations and the similarity in observed phases and amplitudes suggest a dominant global mode. For the ter-diurnal tide, this dominant mode likely shifts between TW3 and TE3, and is strongly influenced by water ice clouds.

5 Summary and Discussion

Atmospheric tides on various Martian landing sites was investigated by studying the ter-diurnal (8 hr) harmonic component. This study is a continuation of our previous work (Leino et al., 2023) which was associated with the two strongest component, diurnal and semi-diurnal tides near the equator.

In this investigation we use hourly binned surface pressure observations by MSL, InSight, VL1, and VL2 to calculate harmonic components with FFT for each location, focusing on the ter-diurnal tidal component. We studied the sensitivity of the component to the location, season, and atmospheric dust content. In addition, we made global model predictions using MCD and compared the results with observations as well as studied the effect of water ice clouds.

MSL and InSight showed very similar seasonal cycles with highest ter-diurnal amplitudes at about Ls 60°, Ls 130°, and Ls 320°. The latest amplitude peak corresponds to a "C" dust storm (Kass et al., 2016) and is also visible in the diurnal and semi-diurnal tidal amplitudes (Leino et al., 2023). Observed VL1 and VL2 ter-diurnal amplitudes seem to be lacking a clear structure, but VL1 showed quite repeatable and similar pattern as MSL and InSight during the first half of the year. In addition, global dust storms during MY 12 (1977b) and 15 were clearly detected by the ter-diurnal tide amplitude. However, ter-diurnal amplitude did not show a clear response during the 1977a planet-encircling dust storm. The global dust storm during MY 34 was visible in the MSL pressure data demonstrating the highest ter-diurnal amplitude during the MSL mission by now.

MSL and InSight showed very similar pattern in ter-diurnal phases as well, with values between 05–07 LTST most of the year and 08–10 LTST during Ls 60°–120°. Phases observed by the Viking Landers were lacking a clear structure, but VL1 showed some pattern at the start of the year. The phases predicted by the MCD data were in quite good agreement with observations, except for the MSL.

Overall, calculations on MCD pressure data seem to underestimate ter-diurnal amplitudes throughout the year, especially during the dusty season. MCD predicted weakest amplitudes at the equinoxes, while strongest ones were predicted in summertime for both hemispheres with a clear wavenumber 6 pattern in longitude during Ls 60°–150°. This wavenumber pattern was produced by the interaction between TW3 and TE3 tides. It may be concluded that ter-diurnal tide is much more complex compared to the diurnal and semi-diurnal tides.

This study suggests that ter-diurnal amplitude is very sensitive to column water ice. This is indicated by our calculations with MCD data which suggest high sensitivity to column water ice during the northern hemisphere summer, while MCD amplitudes follow more airborne dust conditions after that. MSL and InSight both observed peaks

in the amplitude of the ter-diurnal tidal component during the seasonal "C" dust storm (at about Ls 320°) each year. However, during the "A" dust storm (at about Ls 230°) neither platforms detected amplitude spikes. This behavior may be related to different vertical distribution of dust during these storms, but clearly more studies are needed.

GCM simulations with and without radiative active water ice clouds suggest that TE3 mode amplitude peaks at the equator and is much less prominent without radiatively active water ice clouds. Moreover, the observed delay and advance of the ter-diurnal phase, as well as the amplitude patterns indicate that the TE3 mode has a characteristic of the resonantly-enhanced ter-diurnal Kelvin wave. Interaction between solar radiation and zonal wave 6 variations in topography and surface properties (thermal inertia and albedo) may generate this mode. When, TW3 tide was stronger away from the equator and was present for a much longer fraction of the year. This component may be a result of direct solar forcing or nonlinear interaction between diurnal and semi-diurnal tides.

Moreover, ter-diurnal amplitude and phase observed by Perseverance (Fig. 7, Harri et al., 2024) are consistent with the results seen at the MSL/InSight location, buttressing the argument that these are all manifestations of global scale tides. Similar phase deviations seen in the Perseverance data suggest the presence of the enhanced ter-diurnal Kelvin wave. Since Perseverance and MSL/InSight are separated by 60 degrees of longitude the phase deviation due to the Kelvin wave would be similar at the 3 locations, as seen in the data. Moreover, similar signs of phase delay and advance observed by VL1 also support the increased presence of the resonantly-enhanced ter-diurnal Kelvin wave as MSL/InSight and VL1 are separated by about 180 degrees of longitude.

Based on this investigation, it seems to be reasonable to infer that ter-diurnal tide has a seasonal cycle at least near the equator, which is strongly influenced by water ice clouds. Nonetheless, the amplitude is typically lower than that for the diurnal and semi-diurnal tides. Definitely more modeling studies are needed to understand the behavior and forcing mechanisms of this important component of the Martian atmospheric tide.

Open Research Section

VL1 (PDS3 format), VL2 (PDS3 format), MSL (PDS3 format), and InSight (PDS4 format) pressure data are freely available from the Planetary Data System Atmospheres Node (J. Tillman, 1989; Banfield et al., 2019; Gomez-Elvira, 2013). Atmospheric optical depths are retrieved from MSL Mastcam solar tau imaging sequences following the methodology of Lemmon et al. (2015). Meteorological fields from the Mars Climate Database are available at `http://www-mars.lmd.jussieu.fr/mcd_python/` (Forget et al., 1999; Millour et al., 2017).

Acknowledgments

Joonas Leino, Mark Paton and Ari-Matti Harri are thankful for the Finnish Academy grant numbers 310509 and 357577. Support for R.J. Wilson was provided by NASA's Planetary Science Division Research Program through the Mars Climate Modeling Center (MCMC) Internal Scientist Funding Model (ISFM) work package at Ames Research Center. The authors are greatful to Ehouarn Millour and the LMD team for providing us with additional GCM simulations.

References

Banfield, D., Conrath, B., Pearl, J. C., Smith, M. D., & Christensen, P. (2000). Thermal tides and stationary waves on mars as revealed by mars global surveyor thermal emission spectrometer. *Journal of Geophysical Research: Plan-*

ets, *105*(E4), 9521-9537. doi: https://doi.org/10.1029/1999JE001161

Banfield, D., Mora Sotomayor, L., & Huber, L. (2019). *Insight auxiliary payload sensor subsystem (apss) pressure sensor (ps) archive bundle* [dataset]. doi: https://doi.org/10.17189/1518939

Chamberlain, T. E., Cole, H. L., Dutton, R. G., Greene, G. C., & Tillman, J. E. (1976, 09). atmospheric measurements on Mars: the Viking Meteorology Experiment. *Bulletin of the American Meteorological Society*, *57*(9), 1094-1105. doi: 10.1175/1520-0477(1976)057⟨1094:AMOMTV⟩2.0.CO;2

Chapman, S., & Lindzen, R. (1970). *Atmospheric tides* (Vol. 10). doi: 10.1007/BF00171584

Forbes, J. M., Bridger, A. F. C., Bougher, S. W., Hagan, M. E., Hollingsworth, J. L., Keating, G. M., & Murphy, J. (2002). Nonmigrating tides in the thermosphere of mars. *Journal of Geophysical Research: Planets*, *107*(E11), 23-1-23-12. Retrieved from `https://agupubs.onlinelibrary.wiley.com/doi/abs/10.1029/2001JE001582` doi: https://doi.org/10.1029/2001JE001582

Forget, F., Hourdin, F., Fournier, R., Hourdin, C., Talagrand, O., Collins, M., ... Huot, J.-P. (1999, October). Improved general circulation models of the Martian atmosphere from the surface to above 80 km. *Journal of Geophysical Research, Volume 104, Issue E10, p. 24155-24176*, *104*(E10), 24155-24176. doi: 10.1029/1999JE001025

Gómez-Elvira, J., Armiens, C., Castañer, L., Domínguez, M., Genzer, M., Gómez, F., ... Martín-Torres, J. (2012, August). REMS: The Environmental Sensor Suite for the Mars Science Laboratory Rover. *Space Sci. Rev.*, *170*(1-4), 583-640. doi: 10.1007/s11214-012-9921-1

Gomez-Elvira, J. (2013). *Mars science laboratory rover environmental monitoring station rdr data v1.0, msl-m-rems-5-modrdr-v1.0, nasa planetary data system* [dataset]. doi: https://doi.org/10.17189/1523033

Groves, G. V., & Wilson, A. (1982, July). Diurnal, semi-diurnal and terdiurnal Hough components of surface pressure. *Journal of Atmospheric and Terrestrial Physics*, *44*(7), 599-611. doi: 10.1016/0021-9169(82)90071-X

Guzewich, S. D., Newman, C., de la Torre Juárez, M., Wilson, R., Lemmon, M., Smith, M., ... Harri, A.-M. (2016). Atmospheric tides in gale crater, mars. *Icarus*, *268*, 37-49. Retrieved from `https://www.sciencedirect.com/science/article/pii/S0019103515005850` doi: https://doi.org/10.1016/j.icarus.2015.12.028

Hagan, M. E., & Roble, R. G. (2001). Modeling diurnal tidal variability with the national center for atmospheric research thermosphere-ionosphere-mesosphere-electrodynamics general circulation model. *Journal of Geophysical Research: Space Physics*, *106*(A11), 24869-24882. doi: https://doi.org/10.1029/2001JA000057

Hamilton, K. (1982). The effect of solar tides on the general circulation of the martian atmosphere. *Journal of Atmospheric Sciences*, *39*(3), 481 - 485. doi: 10.1175/1520-0469(1982)039⟨0481:TEOSTO⟩2.0.CO;2

Harri, A.-M., Genzer, M., Kemppinen, O., Kahanpää, H., Gomez-Elvira, J., Rodriguez-Manfredi, J. A., ... the REMS/MSL Science Team (2014). Pressure observations by the curiosity rover: Initial results. *Journal of Geophysical Research: Planets*, *119*(1), 82-92. doi: 10.1002/2013JE004423

Harri, A.-M., Paton, M., Hieta, M., Polkko, J., Newman, C., Pla-Garcia, J., ... Martinez, G. (2024). Perseverance meda atmospheric pressure observations—initial results. *Journal of Geophysical Research: Planets*, *129*(3), e2023JE007880. Retrieved from `https://agupubs.onlinelibrary.wiley.com/doi/abs/10.1029/2023JE007880` (e2023JE007880 2023JE007880) doi: https://doi.org/10.1029/2023JE007880

Hess, S. L., Henry, R. M., Leovy, C. B., Ryan, J. A., & Tillman, J. E. (1977). Meteorological results from the surface of mars: Viking 1 and 2. *Jour-*

nal of Geophysical Research (1896-1977), *82*(28), 4559-4574. doi: 10.1029/JS082i028p04559

Kass, D. M., Kleinböhl, A., McCleese, D. J., Schofield, J. T., & Smith, M. D. (2016). Interannual similarity in the martian atmosphere during the dust storm season. *Geophysical Research Letters*, *43*(12), 6111-6118. Retrieved from https://agupubs.onlinelibrary.wiley.com/doi/abs/10.1002/2016GL068978 doi: https://doi.org/10.1002/2016GL068978

Leino, J., Harri, A.-M., Banfield, D., de la Torre Juárez, M., Paton, M., Rodriguez-Manfredi, J.-A., ... Savijärvi, H. (2023). Martian equatorial atmospheric tides from surface observations. *Journal of Geophysical Research: Planets*, *128*(10), e2023JE007957. Retrieved from https://agupubs.onlinelibrary.wiley.com/doi/abs/10.1029/2023JE007957 (e2023JE007957 2023JE007957) doi: https://doi.org/10.1029/2023JE007957

Lemmon, M. T., Wolff, M. J., Bell, J. F., Smith, M. D., Cantor, B. A., & Smith, P. H. (2015). Dust aerosol, clouds, and the atmospheric optical depth record over 5 mars years of the mars exploration rover mission. *Icarus*, *251*, 96-111. Retrieved from https://www.sciencedirect.com/science/article/pii/S0019103514001559 (Dynamic Mars) doi: https://doi.org/10.1016/j.icarus.2014.03.029

Leovy, C., & Zurek, R. (1979, 07). Thermal tides and martian dust storms - direct evidence for coupling. *J. Geophys. Res.*, *84*. doi: 10.1029/JB084iB06p02956

Leovy, C. B. (1981). Observations of martian tides over two annual cycles. *Journal of Atmospheric Sciences*, *38*(1), 30 - 39. doi: 10.1175/1520-0469(1981)038⟨0030:OOMTOT⟩2.0.CO;2

Millour, E., Forget, F., Spiga, A., Vals, M., Zakharov, V., Navarro, T., ... MCD/GCM Development Team (2017). The Mars Climate Database (MCD version 5.3). In *Egu general assembly conference abstracts* (p. 12247).

Montabone, L., Forget, F., Millour, E., Wilson, R., Lewis, S., Cantor, B., ... Wolff, M. (2015). Eight-year climatology of dust optical depth on mars. *Icarus*, *251*, 65-95. Retrieved from https://www.sciencedirect.com/science/article/pii/S0019103515000044 (Dynamic Mars) doi: https://doi.org/10.1016/j.icarus.2014.12.034

Montabone, L., Spiga, A., Kass, D. M., Kleinböhl, A., Forget, F., & Millour, E. (2020). Martian year 34 column dust climatology from mars climate sounder observations: Reconstructed maps and model simulations. *Journal of Geophysical Research: Planets*, *125*(8), e2019JE006111. Retrieved from https://agupubs.onlinelibrary.wiley.com/doi/abs/10.1029/2019JE006111 (e2019JE006111 10.1029/2019JE006111) doi: https://doi.org/10.1029/2019JE006111

Moudden, Y., & Forbes, J. M. (2013). A decade-long climatology of terdiurnal tides using timed/saber observations. *Journal of Geophysical Research: Space Physics*, *118*(7), 4534-4550. Retrieved from https://agupubs.onlinelibrary.wiley.com/doi/abs/10.1002/jgra.50273 doi: https://doi.org/10.1002/jgra.50273

Ray, R. D., Boy, J.-P., Erofeeva, S. Y., & Egbert, G. D. (2023). Terdiurnal radiational tides. *Journal of Physical Oceanography*, *53*(4), 1139 - 1150. Retrieved from https://journals.ametsoc.org/view/journals/phoc/53/4/JPO-D-22-0175.1.xml doi: https://doi.org/10.1175/JPO-D-22-0175.1

Read, P. L., & Lewis, S. R. (2004). *The martian climate revisited: atmosphere and environment of a desert planet* (Vol. 26). Springer.

Siebert, M. (1961, January). Atmospheric Tides. *Advances in Geophysics*, *7*, 105. doi: 10.1016/S0065-2687(08)60362-3

Smith, A. K. (2000). Structure of the terdiurnal tide at 95 km. *Geophysical Research Letters*, *27*(2), 177-180. Retrieved from https://agupubs.onlinelibrary.wiley.com/doi/abs/10.1029/1999GL010843 doi:

https://doi.org/10.1029/1999GL010843

Spiga, A., Banfield, D., Teanby, N. A., Forget, F., Lucas, A., Kenda, B., ... Banerdt, W. B. (2018, October). Atmospheric Science with InSight. *Space Science Reviews*, *214*(7), 109. doi: 10.1007/s11214-018-0543-0

Spiga, A., Murdoch, N., Lorenz, R., Forget, F., Newman, C., Rodriguez, S., ... Banerdt, W. B. (2021). A study of daytime convective vortices and turbulence in the martian planetary boundary layer based on half-a-year of insight atmospheric measurements and large-eddy simulations. *Journal of Geophysical Research: Planets*, *126*(1), e2020JE006511. Retrieved from `https://agupubs.onlinelibrary.wiley.com/doi/abs/10.1029/2020JE006511` (e2020JE006511 2020JE006511) doi: https://doi.org/10.1029/2020JE006511

Tillman, J. (1989). *Vl1/vl2-m-met-3-p-v1.0, nasa planetary data system* [dataset].

Tillman, J. E., Johnson, N. C., Guttorp, P., & Percival, D. B. (1993). The martian annual atmospheric pressure cycle: Years without great dust storms. *Journal of Geophysical Research: Planets*, *98*(E6), 10963-10971. Retrieved from `https://agupubs.onlinelibrary.wiley.com/doi/abs/10.1029/93JE01084` doi: https://doi.org/10.1029/93JE01084

Viúdez-Moreiras, D., Newman, C. E., Forget, F., Lemmon, M., Banfield, D., Spiga, A., ... the TWINS/InSight team (2020). Effects of a large dust storm in the near-surface atmosphere as measured by insight in elysium planitia, mars. comparison with contemporaneous measurements by mars science laboratory. *Journal of Geophysical Research: Planets*, *125*(9), e2020JE006493. Retrieved from `https://agupubs.onlinelibrary.wiley.com/doi/abs/10.1029/2020JE006493` (e2020JE006493 2020JE006493) doi: https://doi.org/10.1029/2020JE006493

Wilson, R., & Kahre, M. (2022). A network of surface pressure observations to constrain aerosol forcing in Mars climate models. In *7th international workshop on the mars atmosphere: Modeling and observations, paris, france.*

Wilson, R., Murphy, J., & Tyler, D. (2017). Assessing atmospheric thermal forcing from surface pressure data: Separating thermal tides and local topographic influence. In *Mars atmosphere: Modeling and observations, 6th international workshop, granada, spain.*

Wilson, R. J., & Hamilton, K. (1996). Comprehensive model simulation of thermal tides in the martian atmosphere. *Journal of Atmospheric Sciences*, *53*(9), 1290 - 1326. doi: 10.1175/1520-0469(1996)053⟨1290:CMSOTT⟩2.0.CO;2

Zurek, R. (1976, 03). Diurnal tide in the martian atmosphere. *Journal of the Atmospheric Sciences*, *33*. doi: 10.1175/1520-0469(1976)033⟨0321:DTITMA⟩2.0.CO;2

Zurita-Zurita, S., de la Torre Juárez, M., Newman, C. E., Viúdez-Moreiras, D., Kahanpää, H. T., Harri, A.-M., ... Rodríguez-Manfredi, J. A. (2022). Mars surface pressure oscillations as precursors of large dust storms reaching gale. *Journal of Geophysical Research: Planets*, *127*(8), e2021JE007005. Retrieved from `https://agupubs.onlinelibrary.wiley.com/doi/abs/10.1029/2021JE007005` (e2021JE007005 2021JE007005) doi: https://doi.org/10.1029/2021JE007005